Impact of the reproductive organs on crop BRDF as observed from a UAV

Wenjuan Li, Jingyi Jiang, Marie Weiss, Simon Madec, Franck Tison, Burger Philippe, Alexis Comar, Frédéric Baret

HAL Id: hal-03203368
https://hal.inrae.fr/hal-03203368

Submitted on 24 Apr 2023

1 # Impact of the reproductive organs on crop BRDF as observed

2 # from a UAV

3

4 Wenjuan Li[a,b,1], Jingyi Jiang[a,d,1], Marie Weiss[a], Simon Madec[a], Franck Tison[a], Burger

5 Philippe[c], Alexis Comar[b], Fred Baret[a]

6

7 [a]INRAE, Avignon Université, UMR EMMAH, F-84000, Avignon, France

8 [b]HIPHEN, F-84000, Avignon, France

9 [c]INRAE, UMR AGIR, Toulouse, France

10 [d]Research Center of Forest Management Engineering of State Forestry and Grassland

11 Administration, Beijing Forestry University, 100083, Beijing, China

12

13

14

15

16

17

18

19

20

21

22

23

24 [1] These authors contributed equally.

Highlights

- A UAV equipped with a multispectral camera was used to characterize the impact of reproductive organs on canopy BRDF.

- Ears of wheat, tassels of maize, and heads of sunflower impact canopy reflectance with substantial effect on NDVI.

- 3D simulations of the reproductive organ layer confirm the general trends observed with the UAV.

- Reproductive organs should be accounted for to improve the accuracy of GAI estimates from multispectral reflectance.

Abstract

Several crops bear reproductive organs (RO) at the top of the canopy after the flowering stage, such as ears for wheat, tassels for maize, and heads for sunflowers. RO present specific architecture and optical properties as compared to leaves and stems, which may impact canopy reflectance. This study aims to understand and quantify the influence of RO on the bi-directional variation of canopy reflectance and NDVI.

Multispectral camera observations from a UAV were completed over wheat, maize, and sunflower just after flowering when the RO are fully developed and the leaf layer with only marginal senescence. The flights were designed to sample the BRDF with view zenith angles spanning from nadir to 60° and many compass directions. Three flights corresponding to three sun positions were completed under clear sly conditions. The camera was always pointing to two adjacent plots of few tenths of square meters: the RO were manually removed on one plot, while the other plot was kept undisturbed.

Results showed that the three visible bands (450 nm, 570 nm, 675 nm), and in a lesser way the red edge band (730 nm) were strongly correlated. We, therefore, focused on the 675nm and 850 nm bands. The Bi-Directional Reflectance (BRF) of the canopy without RO shows that the BRF values were almost symmetrical across the principal plane, even for maize and sunflower canopies with a strong row structure. Examination of the BRF difference between the canopy with and without RO indicate that the RO impact canopy BRDF for the three crops. The magnitude of the impacts depends on crop, wavelength and observational geometry. These observations are generally consistent with realistic 3D reflectance simulations. However, some discrepancies were noticed, mainly explained by the small magnitude of the RO effect on canopy BRF, and the approximations made when simulating the RO layer and its coupling with the bottom canopy layer. We finally demonstrated that the

60 RO layer impact the estimates of canopy traits such as GAI as derived from the multispectral

61 observations.

64

65

66

67

1 Introduction

69 Continuous monitoring of crop growth is required for many applications including the

70 evaluation of available resources, precision agriculture (McBRATNEY et al., 2005), and plant

71 phenotyping (Comar et al., 2012). Remote sensing from satellites, planes, or UAVs

72 (Unmanned Aerial Vehicles) are well-suited to describe the crop dynamics from reflectance

73 acquired in several spectral bands. The interpretation of the data in terms of structural and

74 biochemical properties is usually achieved using two main approaches: (1) an empirical

75 approach, based on a set of experiments where both reflectance and canopy characteristics are

76 concurrently measured; (2) a physically based approach using radiative transfer model

77 simulations. For both approaches, assumptions on canopy structure are required to improve

78 the accuracy of canopy characteristics estimates. In the case of the empirical approach,

79 knowledge of the species observed and on the developmental stage may improve the retrieval

80 performances. Similarly, in the case of the physically-based approach, knowledge on the

81 expected range of canopy structure and associated optical properties of the elements may

82 significantly improve the estimates.

83

84   Apart from the canopy structure differences between species, major differences are

85   experienced along the growth cycle because of the appearance of the reproductive organs

86   (RO). RO have structural and optical properties very different from those of the leaves: they

87   are generally thicker than leaves with lower contents in chlorophyll and sometimes elements

88   with specific colors such as petals. These differences are expected to impact the radiative

89   transfer in the canopy significantly since the RO are often located at the top of the canopy to

90   ease pollen and seed dissemination either by the insects, birds, or by the wind. However, only

91   a few studies document the impact of RO on canopy reflectance. Cossani and Reynolds

92   (2012) reported that wheat ears intercept up to 40% of the incident radiation around the

93   flowering stage. Li et al. (2015) show that removing the ear layer at the flowering stage

94   reduces normalized difference vegetation index (NDVI) values by up to 7% in relative values.

95   This explains why Weiss et al. (2001) included explicitly an ear layer to describe the wheat

96   canopy structure and simulate crop reflectance along the growth cycle. Gitelson (2003) and

97   Viña et al. (2004) showed that the presence of the tassels at the top of maize canopies induced

98   a significant decrease of the VARI index. Wanjura and Hatfield (1988) investigated variations

99   in canopy reflectance of sorghum, cotton, and sunflower crops during the growth cycle using

100   the scattering and absorption coefficients. However, they were not able to draw clear

101   conclusions on the impact of sorghum panicles and sunflower heads on canopy reflectance for

102   the Landsat TM bands. More detailed investigations are thus required to better quantify the

103   role of RO on canopy reflectance.

104

105   Canopy reflectance depends on the observational configuration. Therefore, the impact of RO

106   on canopy reflectance should be investigated for the possible view and illumination directions

107   under which crops are usually observed from various remote sensing platforms. Few studies

report detailed measurements of the Bidirectional Reflectance Distribution Function (BRDF) (Nicodemus et al., 1977; Schaepman-Strub et al., 2006) for crops under field conditions. Goniometers have been used in the lab and in the field to characterize the BRDF (Sandmeier and Itten, 1999). However, their use is tedious and time-consuming, while generally corresponding to a very small footprint, questioning its suitability for characterizing the BRDF of tall crops such as maize and sunflower. Alternative airborne instruments such as the Parabola (Deering and Leone, 1986) and Airborne POLDER (Jacob et al., 2002) have been used to measure the BRDF of a range of canopies. They require specific flight design to sample the BRDF over a given target. The recent development of UAVs allows now to easily document the surface BRDF. Different sampling schemes have been used depending on the camera field of view. For a camera equipped with a wide field of view, the UAV is either moving along different tracks to sample the same target from several positions and directions (Hakala et al., 2013) or tilting the camera from about half the total field of view and keeping the UAV at about the same position while rotating in the compass direction (Roosjen et al., 2016). This later technique assumes that the surface is sufficiently homogenous to build the BRDF from points located at different places in the scene. For the small field of view cameras, the UAV is moving around the target while the orientation in view zenith and azimuth is changed continuously to keep the camera pointing towards the target (Burkart et al., 2015, 2014; Grenzdörffer and Niemeyer, 2012). UAVs appear thus very convenient to document the surface BRDF.

Crop 3D modeling offers an efficient way to generate realistic canopies and simulate the associated reflectance for a range of source and view directions (España et al., 1999). Several open-source 3D ray tracing render engines were developed concurrently for computer graphics applications, such as LuxCoreRender (LuxCoreRender, 2018), MITSUBA (Jacob,

6

133   2014), and Pov-ray (POV-team, 2013). They have been successfully used by the remote

134   sensing community to simulate canopy reflectance for a range of vegetation types (Casa and

135   Jones, 2005; Disney et al., 2006; Duthoit et al., 2008; España et al., 1999; Génard et al., 2000;

136   Jiang et al., 2020; Lopez-Lozano et al., 2009). However, most studies focus on crops before

137   the reproductive stage: very few authors have included RO in their simulations due to the

138   complexity of their morphology, topology, and optical properties.

139

140   The objective of this study is to quantify the influence of the RO on canopy BRDF in the

141   visible and near-infrared (NIR) spectral domains. We present a new experimental design to

142   measure canopy BRDF using a multispectral camera onboard an UAV. This allowed

143   evaluating the influence of reproductive organs on the spectral and directional behavior of

144   canopy reflectance. Three main crops are studied, with very different RO at the top of the

145   canopy layer: wheat, maize, and sunflower. Field experiments were conducted for the three

146   species during the reproductive stage to compare the BRDF measured from a UAV between

147   the canopy with and without the RO. These measurements are complemented by reflectance

148   simulations over 3D virtual scenes to better understand and quantify the impact of RO.

149

150   2   Materials and methods

151   2.1   Experimental sites and crops sampled

152   The wheat, maize, and sunflower experiments were located in Avignon, France (43.9°N,

153   4.9°E). The study focused on fully developed crops soon after the flowering stage, when the

154   final height was reached and all leaves were fully developed with only a little senescence

155   appearing at the bottom of the canopy. The wheat (*ISILDUR*) ears were mostly green and

156   bearing awns, the tassels of maize (*Zea mays*) were light yellow. The heads of the sunflower

157 (*MAS 88 OL*) were bearing yellow petals, the flower heads mostly facing the soil. Its back

158 was green, and well seen from the top of the canopy. Note that the rows were oriented East-

159 West for the three experiments (Table 1).

160

161 Table 1. Summary of the flights over wheat, maize, and sunflower experiments. The row

162 azimuth, measurement date, take-off time, average sun zenith (θ_s) and azimuth (φ_s) and

163 illumination conditions during the flight are indicated. The azimuth angles are calculated

164 regarding the North.

165

Species	Date	Row azimuth (°)	Time (GMT+1)	θ_s (°)	φ_s (°)
			15:09	30	226
Wheat	23/05/2017	90.1	16:12	40	246
			09:00	61	91
			14:17	29	221
Maize	08/08/2016	89.2	16:26	44	244
			18:00	61	264
			12:20	30	137
Sunflower	28/07/2017	90.5	10:40	45	108
			09:20	60	89

166
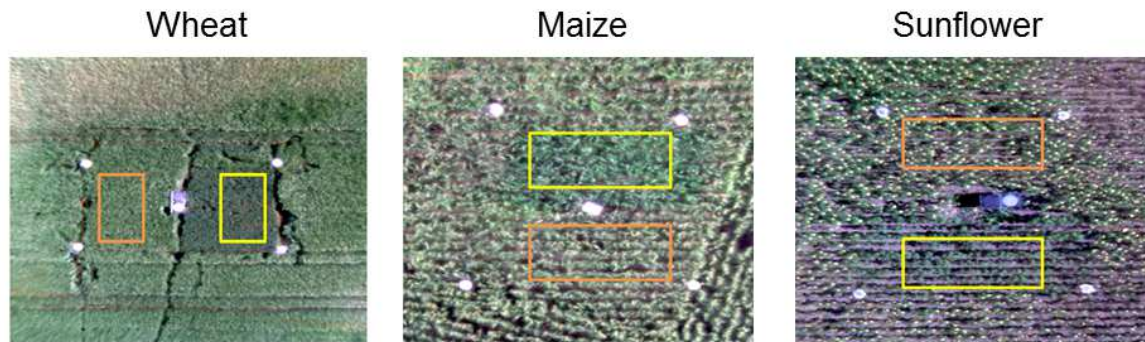
Fig. 1. The three experiments showing the RO+ (with RO, orange rectangle) and RO- (without RO, yellow rectangle) micro plots, the ground control points (GCPs), and the reference panel in the middle.

The sites were selected in a 20 x 20 m homogeneous area of the field. Two micro plots of at least 5 x 5 m² area were considered, one with the RO manually removed (RO-), the other (RO+) being undisturbed (Fig. 1). A 0.6 x 0.6 m² reference panel was placed horizontally slightly higher than the surrounding canopy to avoid possible interactions with the crops and between the two micro plots (Fig. 1). Four circular gray panels of 60 cm diameter were additionally placed on the four corners of the 20 x 20 m² site (Fig. 1) to be used as ground control points (GCP) for accurate projection of the images taken from the UAV. The coordinates of the center of the two reference panels and the four GCPs were measured with an RTK GPS (Trimble Geo 7 ×, 2 cm precision).

2.2 UAV experiment for BRDF characterization

A hexacopter UAV designed by Atechsys (http://atechsys.fr/) was carrying the AIRPHEN multispectral camera (https://www.hiphen-plant.com/our-solutions/airphen/). The camera had 6 spectral bands with 10 nm full width at half maximum. Five bands were equipped with an 8 mm focal length (450 nm, 530 nm, 675 nm, 730 nm, and 850 nm), which provided a field of view (FOV) of $33° × 25°$. The sixth band (570 nm) was equipped with a 4.2 mm focal length providing a $60° × 46°$ FOV. The 4.2 mm lens benefits from a higher overlap (80%) at the

188   expense of a lower spatial resolution (4.06 cm at nadir). It was thus only used to improve the

189   image alignment while the 8 mm lenses for the five other bands were used in the following of

190   the study for their highest spatial resolution (2.11 cm at nadir). Besides the lower spatial

191   resolution, the 4.2 mm lens at 570 nm would not add much spectral information as it is

192   strongly correlated with the 8 mm lens at 530 nm. The camera was triggered every second, the

193   integration time is automatically adjusted using a global shutter. The images were saved into a

194   12 bit TIFF format with metadata information including time of the acquisition, integration

195   time, and GPS coordinates.

196

197   Over each site, the UAV flew three times during the day corresponding approximately to 30°,

198   45°, and 60° nominal sun zenith angles (θ_s) (Table 1). For each θ_s, the UAV sampled five

199   view zenith angles (θ_v = [0°, 15°, 30°, 45°, 60°) for all view azimuth angles (φ_v) by flying

200   along with five concentric circles, each one being at a specific altitude (Fig. 2). Two

201   additional view zenith angles, $\theta_v = \theta_s + 5°$ and $\theta_v = \theta_s - 5°$ were complementing the five

202   nominal θ_v angles to better sample directions close to the hotspot. The flight path was

203   designed before the experiment and included an automatic adjustment of the compass

204   orientation of the camera on the gimbal so that it was always pointing the reference gray

205   panels, the view zenith angle being adjusted for each of the seven circles (Fig. 2). The

206   distance to the ground along the view direction was around 45 m at maximum when cameras

207   were close to the nadir direction (Fig. 2). This provided a ground spatial resolution of about

208   2.11 cm and 4.06 cm respectively for the 8 mm and 4.2 mm focal length. The UAV was

209   flying at about 1m/s speed and it took 7 to 10 minutes to sample all the view directions

210   considered. During the UAV flights, the sky was clear without clouds (Table 1). The wind

211   was gentle for maize and sunflower while significant for wheat with consequences on the

212 faithful realization of the flight plan, with however no severe degradation of the sampling

213 scheme.
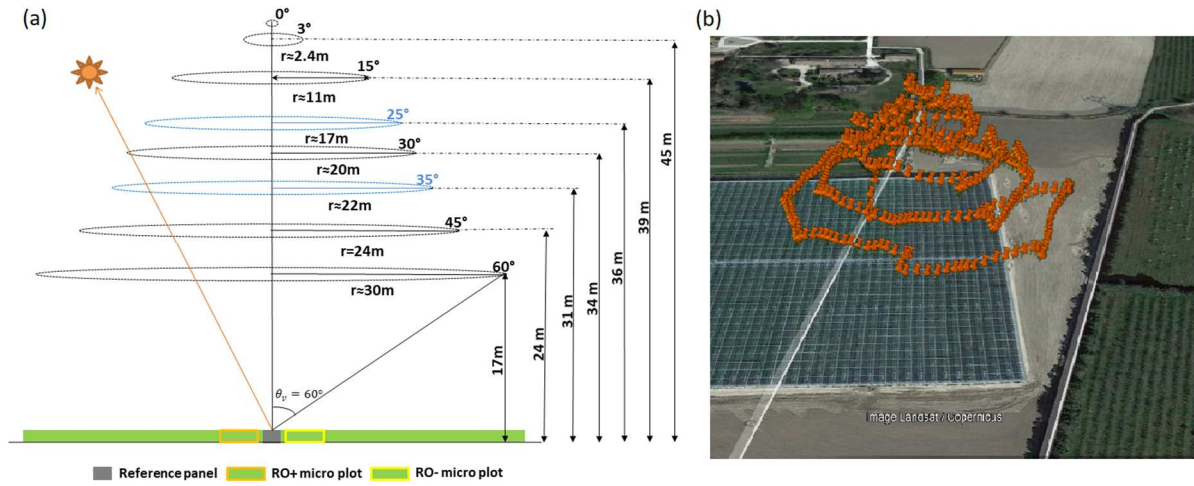
214

215 Fig. 2. (a) The flight plan for $\theta_s = 30°$; (b) the actual flight path over the maize experiment at

216 14:17 local time on 08/08/2016. RO+ and RO- represent micro plots with and without RO,

217 respectively. The background image was from Google Earth[TM].

2.3 Image extraction

219 The raw single frames taken concurrently by the six cameras were firstly co-registered to the

220 reference image at 530 nm using the code developed by Rabatel and Labbé (2015). Vignetting

221 effects were then corrected following the procedure proposed by Verger et al. (2014). Agisoft

222 Photoscan software (Version 1.2.4.2399, Agisoft LLC., Russia) was then run using as input

223 the images taken with the 530 nm and 570 nm cameras equipped respectively with 8 mm and

224 4.2 mm focal lengths. Agisoft Photoscan computed the corresponding position and orientation

225 of the camera for each image. The GCPs were manually identified on the images and used to

226 improve the georeferencing accuracy. The band at 570 nm was not used afterward because of

227 the degraded resolution provided by the 4.2 mm focal length. Furthermore, it was mostly

228 redundant with that at 530 nm with a higher spatial resolution. The pixels corresponding

229 respectively to the two micro plots and the radiometric reference panel were then extracted for

230 the five bands corresponding to the 8 mm focal lengths. The average digital number (DN)

11

value was finally computed and associated with the corresponding integration time (t) and the

view direction (θ_v, φ_v). None of the images used were showing saturated pixels.

2.4 Radiometric calibration

The radiometric reference panel used in the field was made of a gray carpet that was previously characterized in the lab using a goniometer and a white spectralon as primary reflectance reference (Labsphere, Inc., North Sutton, NH, USA). Reflectance measurements were made with a spectral evolution SM-3500 spectrometer (www.spectralevolution.com). The Roujean BRDF model (Roujean et al., 1992) was then adjusted over the goniometer measurements. It was used to simulate the bi-directional reflectance (BRF) of the reference panel for any direction Ω. The 'gray' nature of the panel with all the bands having the same BRF value was well verified (Fig. 3). While the panel was relatively Lambertian for near nadir illumination, significant anisotropy is observed for $\theta_s > 30°$. For this reason, we preferred using only the nadir viewing observations for the radiometric calibration of the camera, assuming that the incoming radiation was stable during the flight.
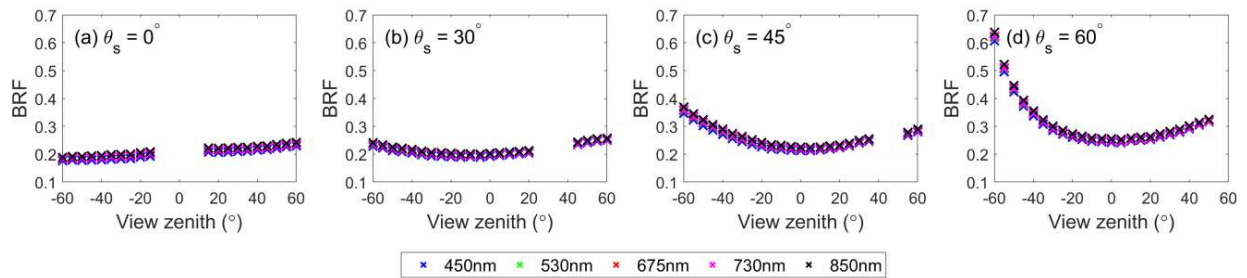
Fig. 3. BRF of the reference panel measured in the lab in the principal plane for four sun zenith angles as a function of the view zenith angle. Positive view zenith angles correspond to the backward direction, while negative values correspond to forward direction.

251   The $BRF\ (\Omega, \lambda)$ of the canopy was computed from the DN values extracted from the images

252   using the known BRF value of the reference panel (BRF_{ref}) and the DN values of the

253   reference panel $DN_{ref}(\Omega, \lambda)$ extracted on the same image (Smith and Milton, 1999) :

254

255   $$BRF\ (\Omega, \lambda) = \frac{DN\ (\Omega,\lambda)/t(\Omega,\lambda)}{DN_{ref}(\Omega o,\lambda)/t_{ref}(\Omega o,\lambda)} BRF_{ref}(\Omega o, \lambda) \tag{1}$$

256

257   where λ is the wavelength, Ω corresponds to the observation configuration with $\Omega =$

258   $[\theta_v, \varphi_v, \theta_s, \varphi_s]$ where θ and φ represent respectively the zenith and azimuth angles, and

259   subscripts v and s correspond respectively to the view and sun directions. *t* is the integration

260   time. The measurements of the reference panel used for the calibration correspond to viewing

261   geometry close to the nadir direction noted here Ωo.

262   The radiance from the reference panel measured in the field includes a contribution of the

263   direct sunlight as well as a diffuse component coming from the light scattered by the sky. The

264   bi-directional reflectance measured in the lab was therefore converted into a blue-sky

265   reflectance factor to account for the diffuse component. The hemispherical-directional

266   reflectance factor was computed based on Roujean's model with the coefficients previously

267   adjusted. The diffuse fraction was finally used to compute the corresponding blue-sky BRF

268   (Schaepman-Strub et al., 2006). The diffuse fraction was derived from the 6S model

269   simulations (Vermote et al., 1997) using the atmospheric characteristics measured from the

270   local AERONET sun photometer as inputs (Holben et al., 1998).

271   Once the BRF at each measurement angle Ω was calculated, they were linearly interpolated

272   from 0° to 60° zenith angles and from 0° to 360° azimuth angles with a 1° step for polar

273   representation. Results are shown in the following analysis for the perpendicular and principal

274   planes.

2.5 Reproductive organs characterization

For each crop, a sample of a representative RO was collected in the field. A set of photos were then taken with a SONY alpha 6000 RGB camera from multiple views: the organ was put vertically over a manually rotating plate in front of a uniform blue background. About 40 to 120 photos were taken by rotating the plate. These multi-view RGB photos were aligned using Agisoft Photoscan software (Version 1.2.4.2399, Agisoft LLC., Russia) to build a dense 3D point cloud used later to model the organ morphology. The lengths of wheat ears and maize tassels and the diameter of sunflower heads were also measured (Table 2). The optical properties in five bands were measured using the AIRPHEN camera: organs were placed horizontally over a black background and viewed from nadir under clear sky field conditions, the sun being at around 45° zenith angle. Organ surface reflectance was then computed using a reference panel placed horizontally in the camera field of view. Average values of sunlit wheat ears, maize tassels, and sunflower petals and front-side and back-side of the heads were then computed (Table 2).

Table 2. Fields and RO characteristics used for the 3D scene generation. The reflectance of sunflower frontside flower and backside flower does not include yellow petals.

Characteristics	Unit	Wheat	Maize	Sunflower
RO- layer height (m)	m	0.8	1.6	1.03
RO- Green Area Index GAI [1]	-	2.7	4.9	0.40
Row spacing (m)	m	0.155	0.77	0.63
Density of RO (nb/m^2)	nb/m²	450	8	4
Length of RO (m)	m	0.11	0.25	
Diameter of RO (m) [2]	m	0.015	0.005	0.25

14

RO area index (m²/m²) [3]	-	1.23	0.16	0.20
Reflectance of RO @675 nm	-	0.1	0.25	Flower front-side: 0.122
				Flower back-side: 0.25
				Flower yellow petal: 0.34
Reflectance of RO @850 nm	-	0.45	0.7	Flower front-side: 0.219
				Flower back-side: 0.5
				Flower yellow petal: 0.36

293 [1] GAI was estimated using a simple empirical model described in Verger et al. (2011) and

294 based on the measured NDVI.

295 [2] Diameter of maize tassel corresponds to the mean value of all branches.

296 [3] RO area of wheat head is calculated as half the developed area of a cylinder. For maize,

297 tassels were considered as made of five cylindric branches. The area of sunflower head was

298 calculated as a disc.

299 **2.6   Reflectance simulations**

300 The canopy was considered as composed of two layers, the top one corresponding to the RO.

301 The bottom layer corresponds to the canopy without the RO. It was characterized by the

302 measured $BRF(\Omega, \lambda)$ value over the RO- modality, with BRF value equal to that measured in

303 the considered view-illumination geometry. The reproductive organ layer was built by

304 replicating the typical reproductive organ (Table 2). For wheat, the ears were vertical and

305 placed regularly according to the plant density For maize, the panicles were randomly

306 oriented and placed according to the row spacing and plant density. For sunflowers, all the

307 flowers were oriented towards the east and placed according to the row spacing and plant

308 density. For the three crops, a small random shift of the nominal position was added to mimic

309 the actual localization of the RO (Fig. 4). Scenes of 2.0 x 2.8 m² were built and replicated 179

310 times around the center one to avoid border effects. The reflectance of the RO material was

15

assumed Lambertian and characterized by the corresponding measured reflectance (Table 2) with transmittance equal to zero.
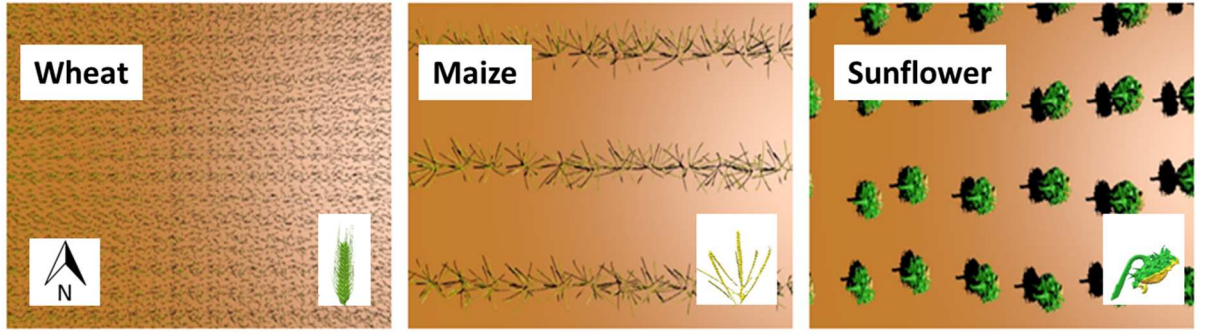
Fig. 4. Nadir view of the 3D scenes (2.0 x 2.8 m²) for wheat, maize, and sunflower as rendered with Luxrender. The sun position is in the east at 45° zenith angle. The reproductive layer was put here on a brown background for better visualization. A side view of the typical reproductive organ replicated in the scene is also displayed for each crop.

Canopy reflectance with RO was simulated using the LuxCoreRender 3D render engine (LuxCoreRender, 2018). LuxCoreRender is open-source software (LuxCoreRender, 2018), which was validated with a set of state-of-the-art models by Jiang et al. (2020) using the RAMI Online Model Checker (ROMC) (Widlowski et al., 2008). We used the LuxCoreRender ray-tracing integrator with 128 rays per camera pixel to guarantee the accuracy of the simulated reflectance. A perspective camera was selected to simulate the AIRPHEN camera with a 33° x 25°field-of-view . For each $\theta_s = [\,30°,\ 45°,\ 60°]$, the observation configuration including $[\theta_v, \varphi_v]$ and the height of the camera was kept the same as in the field experiments. Since the three experiments were conducted under clear sky conditions, no diffuse sky light was considered in our simulations.

3 Results

3.1 Selecting a subset of bands for further analysis

The correlations between the red band (675 nm) and the other four bands were first analyzed to select a subset of bands that will be later investigated for the sake of clarity. Results (Table 3) show that the 450 nm and 530 nm bands were very strongly correlated to the 675 nm band for all sun zenith angles and the three experiments ($r^2 > 0.8$). This is explained by the marginal contribution of multiple scattering and the soil background as well as the fact that most of the elements have similar optical properties in the visible domain. Conversely, bands at 730nm and mainly that at 850 nm show degraded correlations with the visible bands due mostly to the importance of the multiple scattering in the NIR domain. Therefore, we selected the 675 nm and 850 nm bands as a representative subset to illustrate in the following sections the impact of the RO on the directional reflectance.

Table 3. Correlation coefficients (r^2) between canopy reflectance @675 nm and the four other bands for wheat, maize, and sunflower experiments over all images. It includes RO- and RO+ observations for the three sun zenith angles (θ_s).

θ_s		Wheat				Maize				Sunflower			
(°)		450	530	730	850	450	530	730	850	450	530	730	850
RO+	30	0.95	0.95	0.9	0.75	0.99	0.98	0.89	0.65	0.96	0.95	0.72	0.63
	45	0.98	0.96	0.81	0.6	0.99	0.98	0.93	0.76	0.99	0.97	0.88	0.83
	60	1.00	1.00	0.98	0.96	0.99	0.98	0.93	0.8	0.99	0.97	0.91	0.86
RO-	30	0.81	0.91	0.8	0.44	0.99	0.97	0.91	0.66	0.94	0.93	0.8	0.73
	45	0.9	0.92	0.77	0.47	0.99	0.98	0.92	0.75	0.98	0.98	0.92	0.88

| | 60 | 0.97 | 0.98 | 0.93 | 0.84 | 0.99 | 0.96 | 0.89 | 0.68 | 0.98 | 0.98 | 0.94 | 0.89 |

347

3.2 Directional effects over the canopy without the reproductive organs (RO-)

Before quantifying the impact of the reproductive organs on canopy reflectance, the directional properties of the canopies without the RO (RO-) corresponding only to the leaf and stem layer over the soil background were first investigated. They will be used later to compute canopy BRDF using the simulated layer of RO.

3.2.1 Main directional features

The directional features for the three crops and two bands show similar patterns across the three sun positions. We, therefore, illustrate it using only the measurements for $\theta_s = 45°$ (Fig. 5). Measurements for the other two sun directions are presented in Fig. A1 and Fig. A2. The polar plots were obtained by linear interpolation of the raw measured BRF in both zenith and azimuth directions with a $1°$ angular resolution. A peak corresponding to the sun direction is observed in the hotspot, i.e. when the shadows cast by the leaves or soil roughness are not seen (Qin and Goel, 1995). The hotspot is relatively narrow for the maize and sunflower crops both in the red and NIR bands, while it appears broader for te wheat in these two bands. Note that the hotspot is located in the South-Eastern compass directions for the sunflower experiments since measurements were completed in the morning (Table 1). Conversely, the hotspot is in the South-Western compass direction for maize and wheat, corresponding to afternoon flights. For directions opposite to the hotspot corresponding to the forward scattering, the reflectance is generally lower.

367
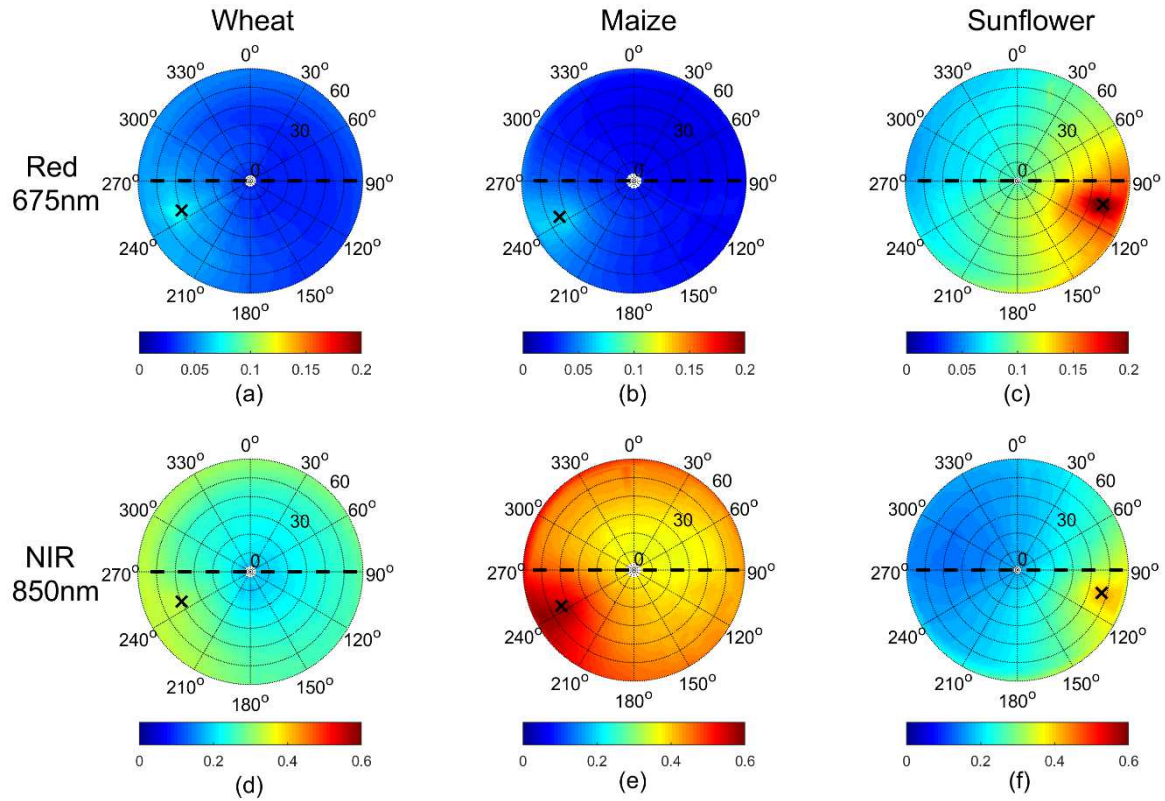
Fig. 5. Polar representation of the measured BRF distribution of the three experiments without the RO (RO-) for 675 nm and 850 nm bands. The sun is displayed as a black cross marker and was at $\theta_s = 45°$. The row orientation (east-west) is represented by the dashed black line. Values represent interpolations from raw measured BRF.

For the visible and NIR bands, the three crops show a general symmetry on both sides of the principal plane, i.e. the plane containing the sun direction (Fig. 5). To better evaluate the symmetry across the principal plane, for each 5° zenith by 5° azimuth cells, the BRF difference, $\delta BRF(\Omega, \lambda)$, with the average of the two symmetrical directions across the principal plane was computed: a perfectly symmetric BRDF with regards to the principal plane should verify $\delta BRF(\Omega, \lambda) = 0$. Results (Fig. 6) confirm that a general symmetry exists across the principal plane since the BRF differences of symmetrical directions are generally within $-0.01 < \delta BRF(\Omega, \lambda) < 0.01$. This is well verified for dense canopies such as maize for both bands (Fig. 6). This is also the case for wheat that presents little row structure at the

19

382   flowering stage. Nevertheless, in the NIR, a slight dissymmetry is observed for the three sun

383   directions, with slightly higher reflectance in the directions north to the principal plane (Fig.

384   6). The sunflower shows very similar patterns in both bands (Fig. 6). A persistent

385   dissymmetry is observed for the three sun positions, with slightly higher reflectance in the

386   directions south to the principal plane. Since the rows were oriented East-West, this can be

387   easily explained for $\theta_s = 30°$ and $\theta_s = 45°$: the illuminated plants and soil in the row are

388   preferentially seen from the southern directions as compared to the northern ones. This agrees

389   very well with the results from (Ranson et al., 1985) as well as reflectance simulations of row

390   canopies (Goel and Grier, 1987; Suits, 1983; Zhao et al., 2010). However, when the sun is

391   almost parallel to the row direction as observed for $\theta_s = 60°$, the southern side appears more

392   reflective than the northern one. This was not expected and is more difficult to explain unless

393   invoking some non-isotropic distribution of leaf azimuthal directions, or some uncorrected

394   biases in the measurements. However, the magnitude of the difference is generally lower than

395   0.01 which is probably close to the measurement uncertainties.

396   Because of the general symmetry across the principal plane, we will focus in the following on

397   the average BRF between the two symmetrical directions across the principal plane. This will

398   offer the advantage to smooth out possible local uncertainties.

399
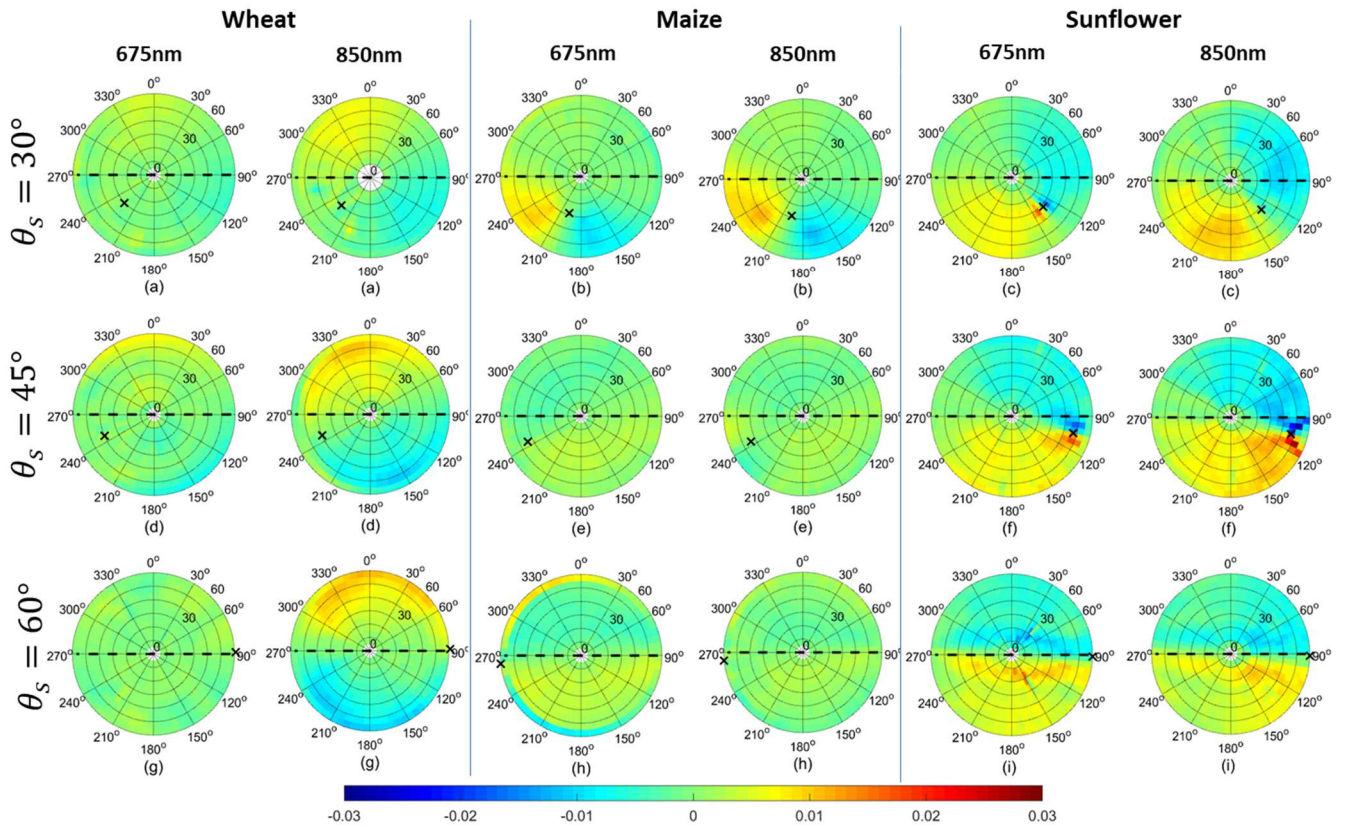
Fig. 6. Polar plot of $\delta BRF(\Omega, \lambda)$ for wheat, maize, and sunflower without RO @675 nm and 850 nm, and the three sun positions considered. $\delta BRF(\Omega, \lambda)$ represents for each view direction the BRF differences with the average BRF values of the two symmetrical directions across the principal plane: when $\delta BRF(\Omega, \lambda) = 0$, the BRF of both symmetrical directions across the principal planes are the same. The black cross marker represents the sun position during the flight. The black dashed line is the row direction.

3.2.2 Directional effects in the principal plane

The BRF in the principal plane was approximated as the BRF measured values within ±5° azimuth difference with that of the sun direction. All the crops, bands, and directions show similar patterns (Fig. 7) with however large differences in magnitude. The maximum BRF is observed always close to the hotspot direction as expected. The minimum BRF values are observed close to the nadir for the NIR band, and in the forward scattering directions for the visible bands. The difference between red and NIR bands depends on the species as a function

414 of the green area index values: the wheat has the largest GAI and the largest difference

415 between red and NIR. Conversely, sunflower has the lowest GAI and the lowest difference

416 between the BRF in both domains. Outside the hotspot directions, small differences of BRFs

417 are observed between the three sun directions with however slightly higher values for $\theta_s =$

418 60° for the more oblique view directions in the NIR, while the contrary is observed in the

419 visible domain (Fig. 7).

420
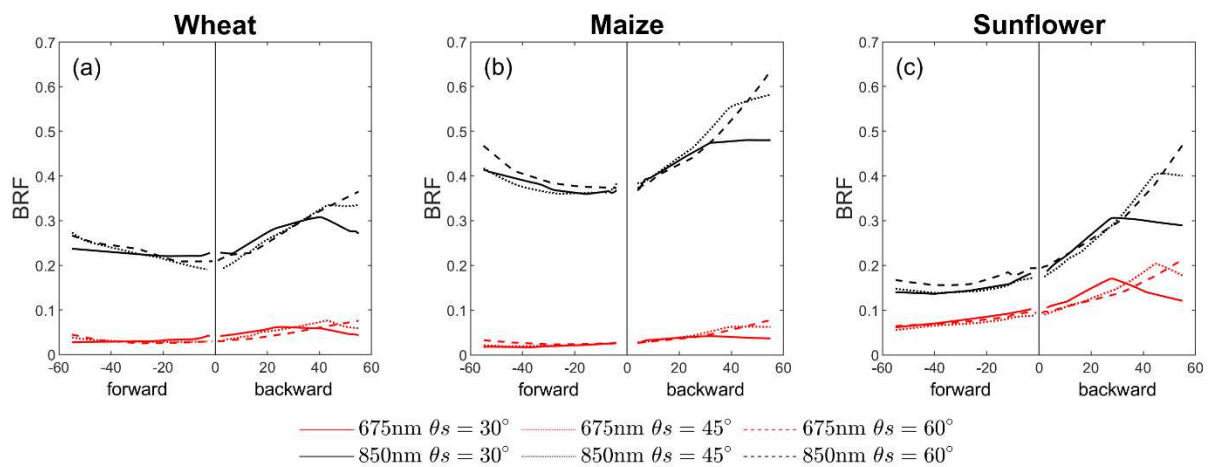
421

422 Fig. 7. BRF values in the red (675 nm) and NIR (850 nm) in the principal plane as a function

423 of the view zenith angles. Observations over canopies without the RO for $\theta_s = [30°, 45°,$

424 60°].

425

426 **3.3   Effects of reproductive organs on canopy reflectance**

427 **3.3.1   Main directional Features**

428 We focused first on $\Delta BRF(\Omega, \lambda)$, i.e. the canopy BRF difference between canopy with organs

429 (RO+) and without organs (RO-). This was computed based on the average BRF between the

430 two symmetrical directions across the principal plane as explained earlier. Results show that

431 the impact of RO on canopy BRF is relatively small in absolute value, with $-0.02 <$

432 $\Delta BRF(\Omega, \lambda) < 0.02$ in the red, and $-0.04 < \Delta BRF(\Omega, \lambda) < 0.04$ in the NIR (Fig. 8).

22

433   However, when computed in relative values, $\Delta BRF(\Omega, \lambda)$ can reach substantial levels up to

434   85% in the red because of the small $BRF(\Omega, \lambda)$ observed (Fig. 5) and up to 34% in the NIR.

435   The impact of RO depends mainly on the crop, on the spectral domain as well as on the

436   directions considered.

437   For wheat, the ears generally decrease canopy reflectance both in the red and NIR bands (Fig.

438   8). This is consistent with studies by Li et al. (2015). Little directional effects due to the sun

439   and view directions are observed, with however larger impacts close to the hotspot. We

440   observe some higher differences (in absolute value) for $\theta_v > 55°$, which may correspond to

441   artifacts in the measurements. Similar artifacts are also noticed for maize and sunflower.

442   The tassels of maize generally increase canopy BRF for all sun and view directions both in

443   the red and NIR domains. The impact increases substantially with the solar zenith angle,

444   while the effect of view direction is marginal (Fig. 8).

445   For sunflower, the influence of heads is contrasted between the red and NIR domains: in the

446   red, the impact is small with $\Delta BRF(\Omega, \lambda) \approx 0$ for the three sun directions; conversely, in the

447   NIR, the heads increase canopy reflectance, particularly for the larger sun zenith angles (Fig.

448   8).
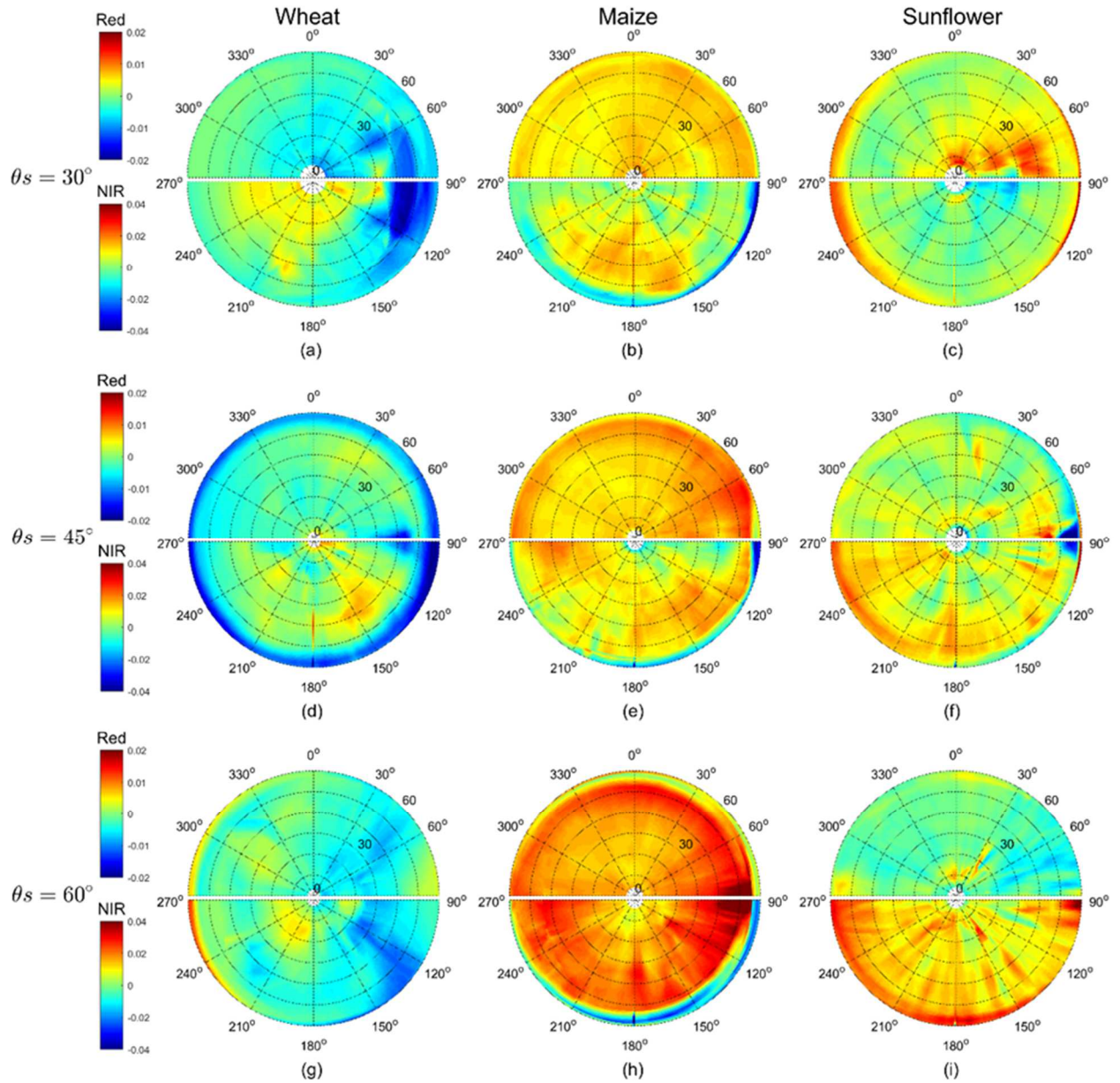
Fig. 8. Directional distribution of $\Delta BRF(\Omega,\lambda)$, the canopy BRF difference with (RO+) and without (RO-) the RO. Wheat (left), maize (middle), and sunflower (right) are displayed for θ_s = [30°,45°,60°]. Each half polar plot represents the average BRF values between the two symmetrical directions across the principal plane. The top hemisphere represents the red band and the bottom one the NIR band. The principal plane is in the 90° - 270° azimuthal direction, with the hotspot located on the right side (90° azimuth).

3.3.2 Consistency between observations and simulations

Since the experimental evidence of the impact of RO on canopy reflectance appears difficult due to the small differences observed and possible confounding measurement uncertainties, we wanted to consolidate the findings based on radiative transfer simulations. We concentrated on the principal plane where most directional features are expected and computed $\Delta BRF(\Omega, \lambda)$.

In the red domain (Fig. 9), simulations confirm that the impact of RO is small. It is slightly negative for wheat, slightly positive for maize, and neglectable for sunflower. For wheat, the addition of the ear layer representing an area index around 1.2 (Table 2) decreases canopy BRF since ears are green with low reflectance (Table 2) without transmitting light, i.e. a very absorbing layer. Furthermore, their vertical position acts as a light trap, increasing light absorption by the lower layers of the canopy. For maize, the tassels act as a scattering layer since they reflect more light than the lower layer of green vegetation due to their higher reflectance (Table 2). When the sun zenith increases, $\Delta BRF(\Omega, \lambda)$ increases because of the longer path length in the tassel layer. The same is also observed for more inclined views, particularly in the backward scattering direction. The small impact of sunflower heads on canopy reflectance can be explained by their small contribution in terms of area index (Table 2), on top of the green layer of leaves. The more subtle differences observed as a function of the observational geometry are difficult to explain.
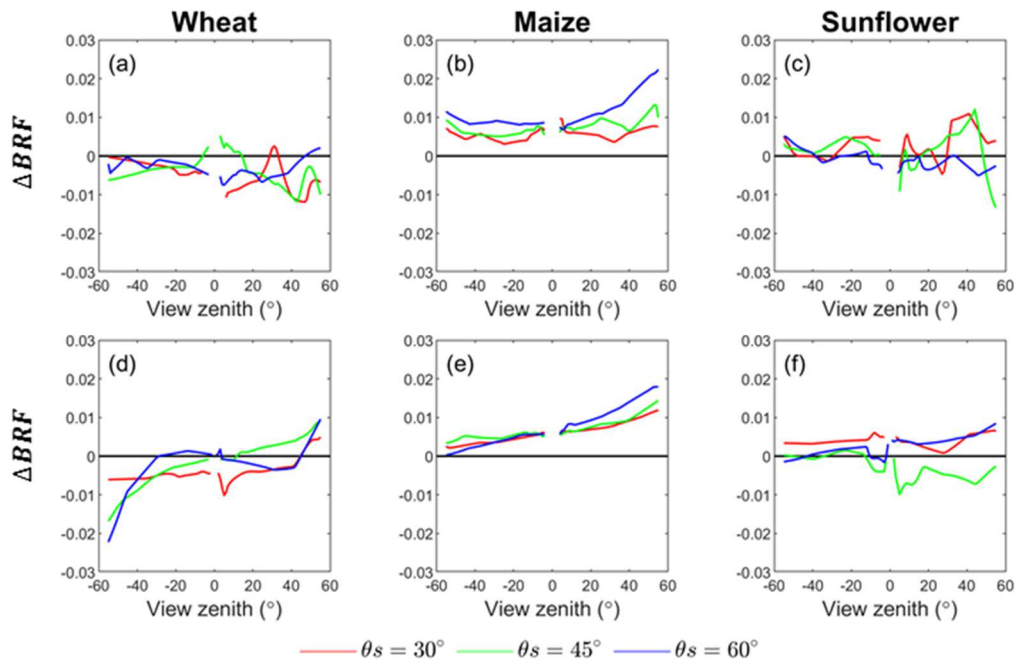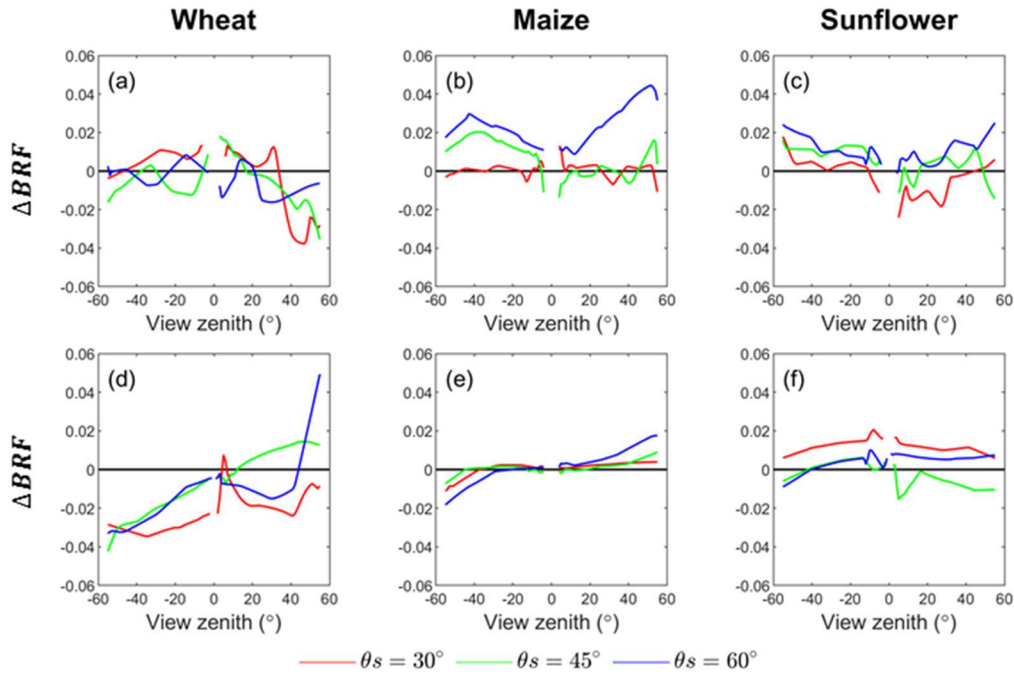
Fig. 9. Measured BRF differences between canopy with (RO+) and without (RO-) RO as a function of the view zenith angle in the principal plane at 675nm from measurements (top) and 3D simulation (bottom). The back-scattering direction corresponds to positive view zenith angles. Crops are shown from left to right: wheat, maize, and sunflower. Several solar zenith angles are considered: $\theta_s = 30°$ (red), $\theta_s = 45°$ (green), and $\theta_s = 60°$ (blue).

In the NIR domain (Fig. 10), the small impact of the ears on $\Delta BRF(\Omega, \lambda)$ is explained by the light trap feature as described previously and the small scattering properties of the ears that do not transmit light. For maize, the discrepancies between measurements and simulations may be partly explained by the fact that the strong row structure of the vegetation layer was not accounted for in our simulations. Measurements show a positive impact of the tassels for $\theta_s = 60°$ and oblique viewing. For the sunflower, the heads induce a slight increase of canopy reflectance, probably due to the high values of the reflectance of the back-side of heads (Table 2) that are pointing upward.

Furthermore, the discrepancies found between observed and simulated $\Delta BRF(\Omega, \lambda)$ values may be explained by the possible measurement uncertainties as well as the assumptions made

493　for the canopy reflectance simulations regarding the spatial homogeneity (i.e. no row

494　structure) of the bottom vegetation layer that is coupled with the RO layer.


495

496　Fig. 10. Measured BRF differences between canopy with and without RO as a function of the

497　view zenith angle in the principle plane at 850nm from measurements (top) and 3D simulation

498　(bottom). The back-scattering direction corresponds to positive view zenith angles. Crops are

499　shown from left to right: wheat, maize, and sunflower (right) and different solar zenith angles

500　are considered: θ_s of 30° (red), 45° (green) and 60° (blue).

3.4　Impact on NDVI values and GAI estimation

502　Previous results demonstrated that the effect of RO on canopy reflectance was variable in the

503　visible and NIR bands. We thus investigated how NDVI (Rouse et al., 1973), a vegetation

504　index widely used to quantify vegetation amount and combining the red and NIR bands, was

505　impacted by the RO. We focused here on near nadir observations ($-10° < \theta_v < 10°$), which

506　is the typical geometry used to observe crops from high-spatial resolution satellites.

507

508

509
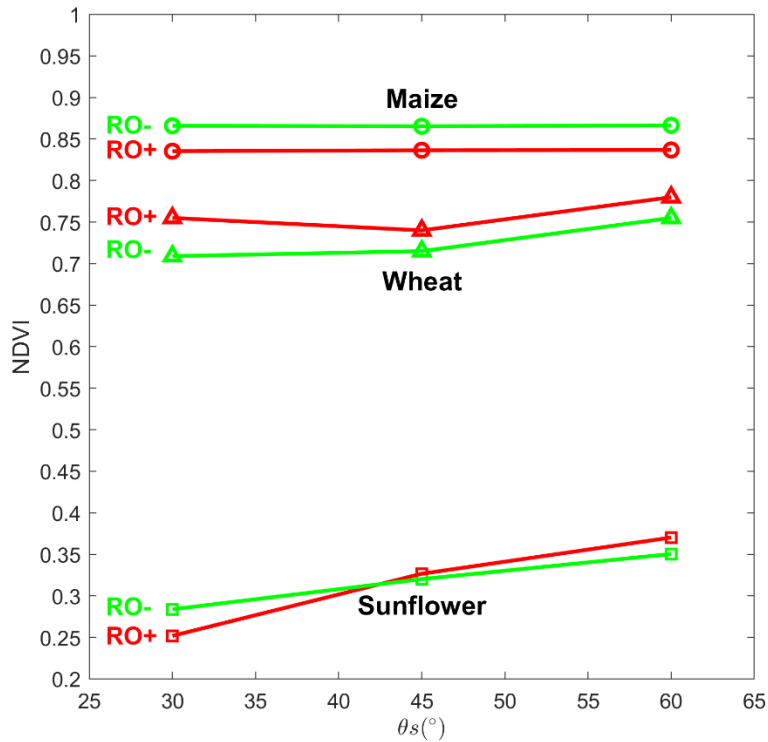
Fig. 11. Variation of NDVI values as observed near nadir (average of BRF for $-10° < \theta_v < 10°$) for maize, sunflower, and wheat with $\theta_s = [30°, 45°, 60°]$. The canopy NDVI values measured with (RO+) and without (RO-) RO are displayed.

513

NDVI indicates the amount of green vegetation that can be also quantified by the green area index (GAI): a gradient is observed between wheat, maize, and sunflower as a function of the GAI value (Table 2), with maize having the larger GAI, and sunflower the lower one (Fig. 11). The addition of ears in wheat canopies increases the NDVI value. This is consistent with the results from Li et al. (2015) and is mainly explained by the green nature of the ears at the flowering stage that absorb strongly in the red and scatter light in the NIR. Note that the area index of the ear layer is close to 1.2 over a GAI of the wheat crop at the flowering stage around 2.7 (Table 2). The variation in NDVI due to the ear layer is around $\Delta NDVI \approx 0.04$. For maize crops, the highly scattering tassels in the red and NIR decrease the NDVI values by $\Delta NDVI \approx -0.03$. These results are consistent with those reported by Gitelson (2003).

28

524 For the sunflower, the impact is slightly negative ($\Delta NDVI \approx -0.02$) for $\theta_s = 30°$ which is

525 explained mainly by the higher scattering properties of the sunflower heads (Table 2).

526 Conversely, the impact is positive ($\Delta NDVI \approx 0.01$) for $\theta_s = 60°$: under this geometry where

527 the sun is parallel to the rows, the heads cast shadows on the row, inducing a larger decrease

528 of the BRF in the red while NIR BRF remains about the same because of the multiple

529 scattering in the canopy. As expected, for medium solar zenith angles ($\theta_s = 45°$) the impact

530 of the heads is intermediate between the two previous situations with $\Delta NDVI \approx 0$.

531

532 Our experimental results also show that the NDVI changes induced by the RO layer can be

533 translated into a change in GAI estimates that can reach up to 25% (Table 4). It can be either

534 positive as in the case of wheat crops and for the sunflower for the smaller solar zenith angle,

535 or negative as in the case of the maize crop.

536

537 Table 4. Impact of the RO on GAI estimates. The measured NDVI values for the canopy with

538 (RO+) and without (RO-) RO are displayed along with the corresponding GAI. The difference

539 is then computed in absolute (ΔGAI) or relative value (ΔGAI %). All GAI values are derived

540 from NDVI using the empirical relationship proposed by Verger et al. (2011).

541

Species	θ_s	RO-		RO+		ΔGAI	ΔGAI %
		NDVI	GAI	NDVI	GAI		
Maize	30°	0.86	4.6	0.83	3.9	-0.7	-15
	45°	0.86	4.6	0.83	3.9	-0.7	-15
	60°	0.87	4.8	0.83	3.9	-1.0	-19
Wheat	30°	0.70	2.2	0.76	2.7	0.5	23
	45°	0.71	2.3	0.74	2.6	0.3	13

	60°	0.76	2.7	0.78	3.1	0.3	15
	30°	0.28	0.4	0.26	0.3	-0.1	-25
Sunflower	45°	0.32	0.5	0.32	0.5	0.0	0
	60°	0.36	0.6	0.37	0.6	0.0	0

542

4 Discussion

4.1 BRF measured by UAVs

We proposed a method to sample the BRDF from UAV multi-angular measurements that appears very efficient as compared to the use of goniometers in the field (Sandmeier and Itten, 1999): it offers the advantage to avoid disturbing the crop surface while using a single footprint where the multiangular observations are concentrated (Roosjen et al., 2016).

Although UAV provides a very promising way to sample the canopy reflectance as demonstrated in this study, uncertainties could be raised in several aspects. We designed carefully the flight plan by taking into account the micro plot size, camera FOV, variation of viewing angles and flight duration. We thus achieved a very good directional sampling of each micro plot. However, around the hotspot direction where very strong variation of canopy reflectance is expected, the sampling density was probably too loose to get a very accurate description of this BRDF feature. Further, the necessary spatial averaging over the microplot induces also a degradation of the directional resolution of the measurements which was around 7°.

Our radiometric calibration based on nadir measurements of the reference panel assumes that the irradiance did not change during the flight. This was preferred as compared to using more frequent observations of the panel under the several view directions sampled un order to reduce the uncertainties attached to the BRDF characterization of the panel as well as the

562　illumination geometry. However, the clear sky conditions and the small time interval

563　necessary to complete the flight (7 ~ 10 minutes) ensured that the illumination conditions

564　were about constant during image acquisition. The method also assumes that the camera

565　responds linearly with the radiance and that the black current is neglectable (Smith and

566　Milton, 1999; Wang and Myint, 2015). Although this was verified for few AIRPHEN

567　cameras, using multiple calibration panels in the field as proposed by Pozo et al., (2014) and

568　Smith and Milton (1999) could allow to confirm this important assumption.

569　4.2　Impact of RO on canopy reflectance and NDVI

570　UAV measurements and 3D model simulations show that the RO have a small effect on the

571　absolute reflectance values, with magnitudes of ±0.02 in the red and ±0.04 in the NIR band

572　(Fig. 8 and Fig. 9). However, expressed in relative values the differences can reach up to 85%

573　in the red and 34% in the NIR. The impact of RO on canopy reflectance vary with crop,

574　spectral bands and show directional effects. This may translate into substantial changes in

575　vegetation index values: for view directions close to nadir, the wheat ears layer increases the

576　NDVI by up to 0.06 (8.57%), while the maize tassels decrease canopy NDVI by up to 0.04

577　(4.60%) (Table 4). The sunflower heads impact differently NDVI depending on sun position

578　due to the complex structure and optical properties of the heads, including difference between

579　the two sides and the presence of yellow petals.

580　These results were derived from measurements acquired at a single date during the crop

581　reproductive stage. However, the impact of RO on reflectance may vary greatly depending on

582　the reproductive stages. For instance, the wheat senescence occurs from the bottom to the top

583　of the canopy and the timing of the disappearance of the chlorophyll pigments in ears will

584　affect the spectral response of the crops (Weiss et al., 2001). Furthermore, the presence of

585　awns, the ear shape or its inclination also vary substantially with the genotype and time, with

586　impact on the spectral and directional behavior on the canopy (Gutierrez et al., 2015).

587   Conversely, for maize, the structure of the tassels is supposed to vary in a lesser extent as

588   compared to wheat, while the yellowing will still have an impact on the spectral variation of

589   the reflectance (Martin et al., 2007). The effect of RO on sunflower reflectance should also be

590   variable depending on the phenological stage as they have the biggest reproductive organs,

591   with contrasted reflectance between each side of the head associated to a complex behavior

592   regarding their orientation due to the heliotropism. Therefore, this study represents a first step

593   to highlight the influence of RO on canopy reflectance but more investigations are required,

594   especially regarding the temporal variations of the spectral properties, the orientation of the

595   organs, genotypic variations and changes in the crop environmental conditions.

596

597   **4.3   Consequences on GAI estimates and applications**

598   The presence of the RO may also impact estimates of GAI. In this study, we used NDVI as a

599   proxy of GAI. Two cases can be considered: (1) if the organs are green and photosynthetically

600   active as in the case of the wheat ears or the sunflower heads, they should be included in the

601   GAI computation since they will contribute to light interception and photosynthesis.

602   However, because the architecture of the reproductive layer at the top of the canopy is

603   different from that of the bottom layer, artifacts may be introduced in the retrieval of GAI if

604   the same architecture is assumed for the two layers. This explains why Weiss et al. (2001)

605   introduced explicitly an ear layer in their dynamic model of wheat canopy architecture. (2) if

606   the RO are not green as for the maize tassels, they will partly absorb and scatter the incoming

607   light without contributing to the GAI. This explains the experimental results from Gitelson et

608   al. (2014) over maize crops who showed that the relationship between the fraction of

609   intercepted radiation and NDVI during the vegetative stage was different from that during the

610   reproductive stage. In both cases, the dynamics of canopy reflectance and NDVI will be

611   altered when the RO are appearing during the flowering stage, leading to possible artifacts on

32

612 GAI estimation. These artifacts introduced by the presence of the RO layer will depend on the

613 specific structural and optical properties features of each genotype. The perturbations in the

614 dynamics due to the apparition of the RO layer offers the potentials to be exploited to date

615 this important growth stage.

5 Acknowledgments

619

6 References

621

622 Anderegg, J., Yu, K., Aasen, H., Walter, A., Liebisch, F., Hund, A., 2020. Spectral Vegetation Indices

623   to Track Senescence Dynamics in Diverse Wheat Germplasm. Front. Plant Sci. 10, 1749.

624   https://doi.org/10.3389/fpls.2019.01749

625 Burkart, A., Aasen, H., Alonso, L., Menz, G., Bareth, G., Rascher, U., 2015. Angular Dependency of

626   Hyperspectral Measurements over Wheat Characterized by a Novel UAV Based Goniometer.

627   Remote Sensing 7, 725–746. https://doi.org/10.3390/rs70100725

628 Burkart, A., Cogliati, S., Schickling, A., Rascher, U., 2014. A Novel UAV-Based Ultra-Light Weight

629   Spectrometer for Field Spectroscopy. IEEE Sensors J. 14, 62–67.

630   https://doi.org/10.1109/JSEN.2013.2279720

631 Casa, R., Jones, H., 2005. LAI retrieval from multiangular image classification and inversion of a ray

632   tracing model. Remote Sensing of Environment 98, 414–428.

633   https://doi.org/10.1016/j.rse.2005.08.005

634 Christopher, J.T., Christopher, M.J., Borrell, A.K., Fletcher, S., Chenu, K., 2016. Stay-green traits to

635   improve wheat adaptation in well-watered and water-limited environments. EXBOTJ 67,

636   5159–5172. https://doi.org/10.1093/jxb/erw276

637 Comar, A., Burger, P., de Solan, B., Baret, F., Daumard, F., Hanocq, J.-F., 2012. A semi-automatic

638   system for high throughput phenotyping wheat cultivars in-field conditions: description and

639   first results. Functional Plant Biol. 39, 914. https://doi.org/10.1071/FP12065

640 Cossani, C.M., Reynolds, M.P., 2012. Physiological Traits for Improving Heat Tolerance in Wheat.

641   Plant Physiol. 160, 1710–1718. https://doi.org/10.1104/pp.112.207753

642 Deering, D., Leone, P., 1986. A sphere-scanning radiometer for rapid directional measurements of sky

643   and ground radiance. Remote Sensing of Environment 19, 1–24. https://doi.org/10.1016/0034-

644   4257(86)90038-6

645 Disney, M., Lewis, P., Saich, P., 2006. 3D modelling of forest canopy structure for remote sensing

646   simulations in the optical and microwave domains. Remote Sensing of Environment 100, 114–

647   132. https://doi.org/10.1016/j.rse.2005.10.003

648 Duan, T., Chapman, S.C., Guo, Y., Zheng, B., 2017. Dynamic monitoring of NDVI in wheat

649   agronomy and breeding trials using an unmanned aerial vehicle. Field Crops Research 210,

650   71–80. https://doi.org/10.1016/j.fcr.2017.05.025

651 Duthoit, S., Demarez, V., Gastellu-Etchegorry, J.-P., Martin, E., Roujean, J.-L., 2008. Assessing the

652   effects of the clumping phenomenon on BRDF of a maize crop based on 3D numerical scenes

653   using   DART   model.   Agricultural   and   Forest   Meteorology   148,   1341–1352.

654   https://doi.org/10.1016/j.agrformet.2008.03.011

655 España, M.L., Baret, F., Aries, F., Chelle, M., Andrieu, B., Prévot, L., 1999. Modeling maize canopy

656   3D architecture Application to reflectance simulation. Ecological Modelling 122, 25–43.

657 Génard, M., Baret, F., Simon, D., 2000. A 3D peach canopy model used to evaluate the effect of tree

658   architecture and density on photosynthesis at a range of scales. Ecological Modelling 128,

659   197–209.

660 Gitelson, A.A., 2003. Novel technique for remote estimation of CO_2 flux in maize. Geophys. Res.

661   Lett. 30, 1486. https://doi.org/10.1029/2002GL016543

662 Gitelson, A.A., Peng, Y., Arkebauer, T.J., Schepers, J., 2014. Relationships between gross primary
663   production, green LAI, and canopy chlorophyll content in maize: Implications for remote
664   sensing of primary production. Remote Sensing of Environment 144, 65–72.
665   https://doi.org/10.1016/j.rse.2014.01.004

666 Goel, N.S., Grier, T., 1987. Estimation of canopy parameters of row planted vegetation canopies using
667   reflectance data for only four view directions. Remote Sensing of Environment 21, 37–51.
668   https://doi.org/10.1016/0034-4257(87)90005-8

669 Gregersen, P.L., Culetic, A., Boschian, L., Krupinska, K., 2013. Plant senescence and crop
670   productivity. Plant Mol Biol 82, 603–622. https://doi.org/10.1007/s11103-013-0013-8

671 Grenzdörffer, G.J., Niemeyer, F., 2012. UAV BASED BRDF-MEASUREMENTS OF
672   AGRICULTURAL SURFACES WITH PFIFFIKUS. Int. Arch. Photogramm. Remote Sens.
673   Spatial Inf. Sci. XXXVIII-1/C22, 229–234. https://doi.org/10.5194/isprsarchives-XXXVIII-1-
674   C22-229-2011

675 Gutierrez, M., Reynolds, M.P., Klatt, A.R., 2015. Effect of leaf and spike morphological traits on the
676   relationship between spectral reflectance indices and yield in wheat. International Journal of
677   Remote Sensing 36, 701–718. https://doi.org/10.1080/01431161.2014.999878

678 Hakala, T., Honkavaara, E., Saari, H., Mäkynen, J., Kaivosoja, J., Pesonen, L., Pölönen, I., 2013.
679   SPECTRAL IMAGING FROM UAVS UNDER VARYING ILLUMINATION
680   CONDITIONS. Int. Arch. Photogramm. Remote Sens. Spatial Inf. Sci. XL-1/W2, 189–194.
681   https://doi.org/10.5194/isprsarchives-XL-1-W2-189-2013

682 Holben, B.N., Eck, T.F., Slutsker, I., Tanré, D., Buis, J.P., Setzer, A., Vermote, E., Reagan, J.A.,
683   Kaufman, Y.J., Nakajima, T., Lavenu, F., Jankowiak, I., Smirnov, A., 1998. AERONET—A
684   Federated Instrument Network and Data Archive for Aerosol Characterization. Remote
685   Sensing of Environment 66, 1–16. https://doi.org/10.1016/S0034-4257(98)00031-5

686 Iqbal, F., Lucieer, A., Barry, K., 2018. Simplified radiometric calibration for UAS-mounted
687   multispectral sensor. European Journal of Remote Sensing 51, 301–313.
688   https://doi.org/10.1080/22797254.2018.1432293

689   Jacob, F., Olioso, A., Weiss, M., Baret, F., Hautecoeur, O., 2002. Mapping short-wave albedo of

690   agricultural surfaces using airborne PolDER data. Remote Sensing of Environment 80, 36–46.

691   https://doi.org/10.1016/S0034-4257(01)00265-6

692   Jacob, W., 2014. Mitsuba Documentation Version 0.5.0 [WWW Document]. URL

693   https://www.mitsuba-renderer.org/

694   Jiang, J., Weiss, M., Liu, S., Rochdi, N., Baret, F., 2020. Speeding up 3D radiative transfer

695   simulations: A physically based metamodel of canopy reflectance dependency on wavelength,

696   leaf biochemical composition and soil reflectance. Remote Sensing of Environment 237,

697   111614. https://doi.org/10.1016/j.rse.2019.111614

698   Li, H., Zhao, C., Yang, G., Feng, H., 2015. Variations in crop variables within wheat canopies and

699   responses of canopy spectral characteristics and derived vegetation indices to different vertical

700   leaf   layers   and   spikes.   Remote   Sensing   of   Environment   169,   358–374.

701   https://doi.org/10.1016/j.rse.2015.08.021

702   Lopez-Lozano, R., Baret, F., García de Cortázar-Atauri, I., Tisseyer, B., Lebon, E., 2009. Reflectance

703   modeling of vineyards under water stress based on the coupling between 3D architecture and

704   water balance model, in: Remote Sensing for Agriculture, Ecosystems, and Hydrology XI.

705   Proceedings of SPIE. Berlin (Germany). https://doi.org/10.1117/12.830057

706   LuxCoreRender,   2018.   LuxCoreRender   Wiki   [WWW   Document].   URL   .

707   https://wiki.luxcorerender.org/LuxCoreRender_Wiki

708   Martin, K.L., Girma, K., Freeman, K.W., Teal, R.K., Stone, M.L., Raun, W.R., 2007. Expression of

709   Variability in Corn as Influenced by Growth Stage Using Optical Sensor Measurements.

710   Agronomy Journal 99, 384–389. https://doi.org/10.2134/agronj2005.0268

711   McBRATNEY, A., Whelan, B., Ancev, T., Mcbratney, A., Bouma, J., 2005. Future Directions of

712   Precision Agriculturew 17.

713   Nicodemus, F.E., Richmond, J.C., Hsia, J.J., Ginsberg, I.W., Limperis, T., 1977. Geometrical

714   considerations and nomenclature for reflectance (No. NBS MONO 160). National Bureau of

715   Standards, Gaithersburg, MD. https://doi.org/10.6028/NBS.MONO.160

716   POV-team, 2013. Introduction to POV-Ray for POV-Ray version 3.7 [WWW Document]. URL

717   http://www.povray.org

718   Pozo, S.D., Rodríguez-Gonzálvez, P., Hernández-López, D., Felipe-García, B., 2014. Vicarious

719   Radiometric Calibration of a Multispectral Camera on Board an Unmanned Aerial System 20.

720   Qin, W., Goel, N.S., 1995. An evaluation of hotspot models for vegetation canopies. Remote Sensing

721   Reviews 13, 121–159. https://doi.org/10.1080/02757259509532299

722   Rabatel, G., Labbé, S., 2015. A fully automatized processing chain for high-resolution multispectral

723   image acquisition of crop parcels by UAV, in: Stafford, J.V. (Ed.), Precision Agriculture '15.

724   Wageningen   Academic   Publishers,   The   Netherlands,   pp.   135–142.

725   https://doi.org/10.3920/978-90-8686-814-8_16

726   Ranson, K.J., Daughtry, C.S.T., Biehl, L.L., Bauer, M.E., 1985. Sun-view angle effects on reflectance

727   factors   of   corn   canopies.   Remote   Sensing   of   Environment   18,   147–161.

728   https://doi.org/10.1016/0034-4257(85)90045-8

729   Roosjen, P., Suomalainen, J., Bartholomeus, H., Clevers, J., 2016. Hyperspectral Reflectance

730   Anisotropy Measurements Using a Pushbroom Spectrometer on an Unmanned Aerial

731   Vehicle—Results for Barley, Winter Wheat, and Potato. Remote Sensing 8, 909.

732   https://doi.org/10.3390/rs8110909

733   Roujean, J.-L., Leroy, M., Deschamps, P.-Y., 1992. A Bidirectional Reflectance Model of the Earth's

734   Surface for the Correction of Remote Sensing Data 97, 20455–20468.

735   Rouse, J.W., Jr., Haas, R.H., Schell, J.A., Deering, D.W., 1973. MOMonitoring vegetation systems in

736   the Great Plains with ERTS. Presented at the Third Earth Resour. Technol. Satell. Symp, pp.

737   309–317. https://doi.org/citeulike-articleid:12009708

738   Sandmeier, S.R., Itten, K.I., 1999. A field goniometer system (FIGOS) for acquisition of hyperspectral

739   BRDF   data.   IEEE   Trans.   Geosci.   Remote   Sensing   37,   978–986.

740   https://doi.org/10.1109/36.752216

741   Schaepman-Strub, G., Schaepman, M.E., Painter, T.H., Dangel, S., Martonchik, J.V., 2006.

742   Reflectance quantities in optical remote sensing—definitions and case studies. Remote

743   Sensing of Environment 103, 27–42. https://doi.org/10.1016/j.rse.2006.03.002

744   Smith, G.M., Milton, E.J., 1999. The use of the empirical line method to calibrate remotely sensed

745   data to reflectance. International Journal of Remote Sensing 20, 2653–2662.

746   https://doi.org/10.1080/014311699211994

747   Suits, G.H., 1983. Extension of a uniform canopy reflectance model to include row effects. Remote

748   Sensing of Environment 13, 113–129. https://doi.org/10.1016/0034-4257(83)90017-2

749   Thomas, H., Smart, C.M., 1993. Crops that stay green. Ann Applied Biology 123, 193–219.

750   https://doi.org/10.1111/j.1744-7348.1993.tb04086.x

751   Verger, A., Baret, F., Camacho, F., 2011. Optimal modalities for radiative transfer-neural network

752   estimation of canopy biophysical characteristics: Evaluation over an agricultural area with

753   CHRIS/PROBA observations. Remote Sensing of Environment 115, 415–426.

754   https://doi.org/10.1016/j.rse.2010.09.012

755   Verger, A., Vigneau, N., Chéron, C., Gilliot, J.-M., Comar, A., Baret, F., 2014. Green area index from

756   an unmanned aerial system over wheat and rapeseed crops. Remote Sensing of Environment

757   152, 654–664. https://doi.org/10.1016/j.rse.2014.06.006

758   Vermote, E.F., Tanre, D., Deuzé, J.L., Herman, M., Morcrette, J.-J., 1997. Second Simulation of the

759   Satellite Signal in the Solar Spectrum, 6S: An Overview. IEEE TRANSACTIONS ON

760   GEOSCIENCE AND REMOTE SENSING 35, 675–686.

761   Viña, A., Gitelson, A.A., Rundquist, D.C., Keydan, G., Leavitt, B., Schepers, J., 2004. Monitoring

762   Maize (*Zea mays* L.) Phenology with Remote Sensing. Agron. J. 96, 1139–1147.

763   https://doi.org/10.2134/agronj2004.1139

764   Wang, C., Myint, S.W., 2015. A Simplified Empirical Line Method of Radiometric Calibration for

765   Small Unmanned Aircraft Systems-Based Remote Sensing. IEEE J. Sel. Top. Appl. Earth

766   Observations Remote Sensing 8, 1876–1885. https://doi.org/10.1109/JSTARS.2015.2422716

767   Wanjura, D.F., Hatfield, J.L., 1988. Vegetative and optical characteristics of four-row crop canopies.

768   International Journal of Remote Sensing 9, 249–258.

769   https://doi.org/10.1080/01431168808954849

770   Weiss, M., Troufleau, D., Baret, F., Chauki, H., Prévot, L., Olioso, A., Bruguier, N., Brisson, N.,

771   2001. Coupling canopy functioning and radiative transfer models for remote sensing data

772   assimilation. Agricultural and Forest Meteorology 108, 113–128.

773   https://doi.org/10.1016/S0168-1923(01)00234-9

774 Widlowski, J.-L., Robustelli, M., Disney, M., Gastellu-Etchegorry, J.-P., Lavergne, T., Lewis, P.,

775   North, P.R.J., Pinty, B., Thompson, R., Verstraete, M.M., 2008. The RAMI On-line Model

776   Checker (ROMC): A web-based benchmarking facility for canopy reflectance models.

777   Remote Sensing of Environment 112, 1144–1150. https://doi.org/10.1016/j.rse.2007.07.016

778 Zhao, F., Gu, X., Verhoef, W., Wang, Q., Yu, T., Liu, Q., Huang, H., Qin, W., Chen, L., Zhao, H.,

779   2010. A spectral directional reflectance model of row crops. Remote Sensing of Environment

780   114, 265–285. https://doi.org/10.1016/j.rse.2009.09.018

781

7   Appendix A
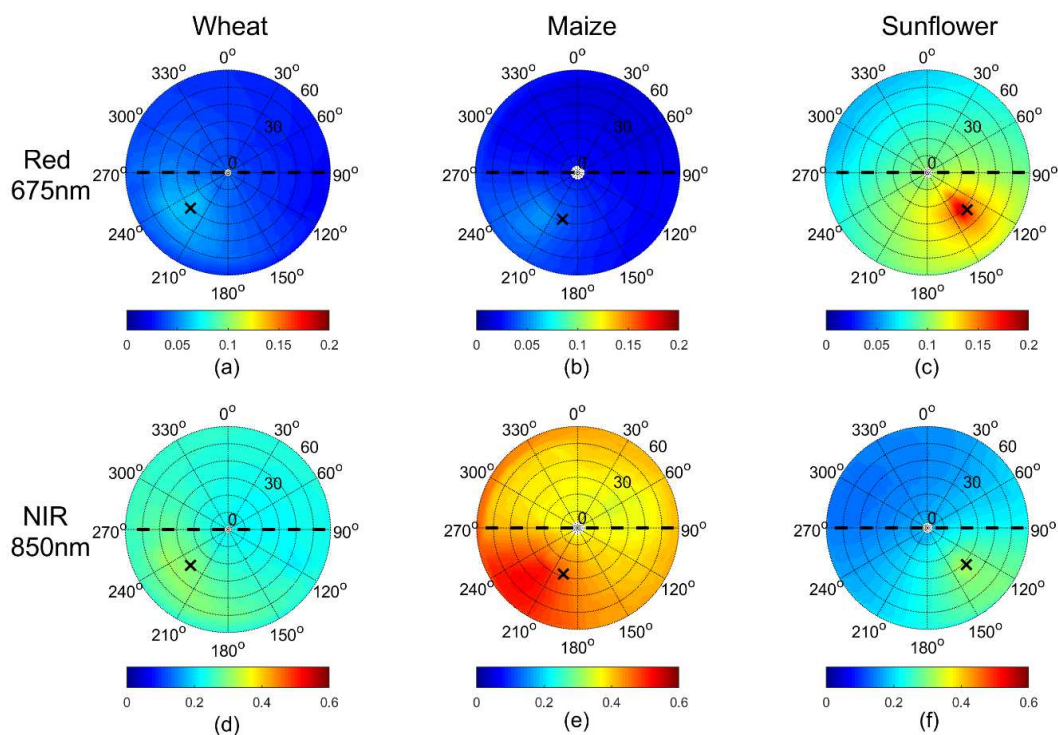
784 Fig. A1. Polar representation of the measured BRF distribution of the three experiments

785 without the RO (RO-) for 675 nm and 850 nm bands. The sun is displayed as a black cross

786   marker and was at $\theta_s = 30°$. The row orientation (east-west) is represented by the dashed

787   black line. Values represent interpolations from raw measured BRF.
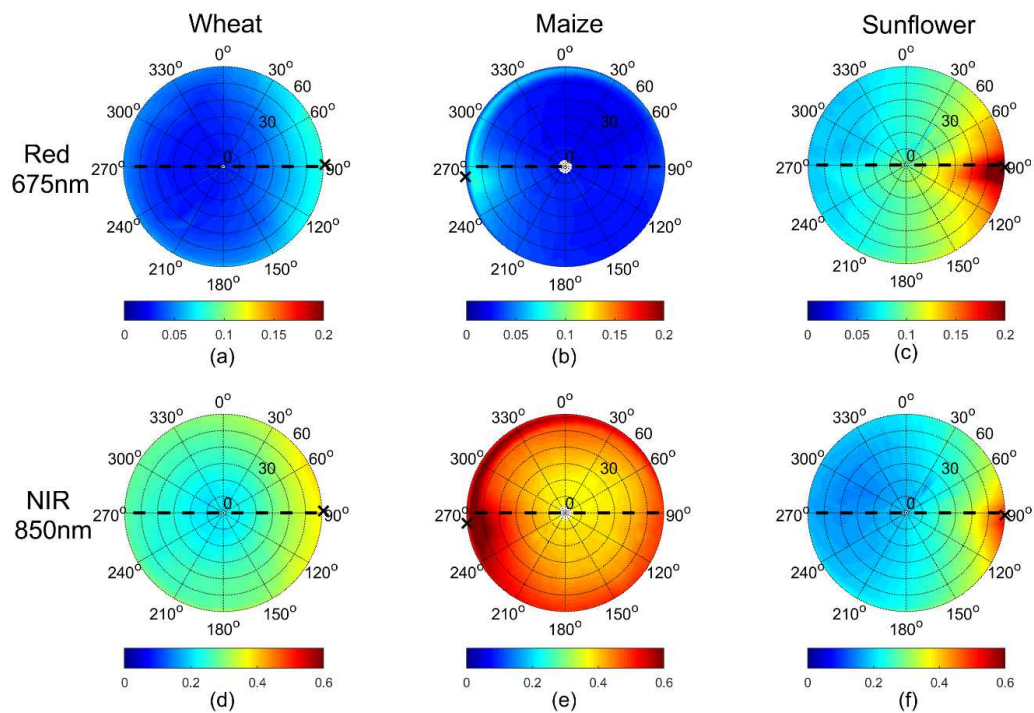
788

789   Fig. A2. Polar representation of the measured BRF distribution of the three experiments

790   without the RO (RO-) for 675 nm and 850 nm bands. The sun is displayed as a black cross

791   marker and was at $\theta_s = 60°$. The row orientation (east-west) is represented by the dashed

792   black line. Values represent interpolations from raw measured BRF.

8 Appendix B

Table B1. Measured reflectance of wheat ears, maize tassels, and sunflower petals, front-side and back-side from AIRPHEN camera on 450nm, 530nm, and 730nm. The reflectance of sunflower frontside flower and backside flower does not include yellow petals.

	450 nm	530 nm	730 nm
Wheat	0.04	0.25	0.35
Maize	0.13	0.2	0.45
Sunflower front-side	0.021	0.10	0.21
Sunflower back-side	0.06	0.17	0.38
Sunflower yellow pedal	0.024	0.27	0.35